A new global model for *P* wave speed variations in Earth's mantle

Chang Li and Robert D. van der Hilst

Department of Earth, Atmospheric, and Planetary Sciences, Massachusetts Institute of Technology, 77 Massachusetts Avenue, Cambridge, Massachusetts 02139, USA (changli@mit.edu)

E. Robert Engdahl

Department of Physics, University of Colorado, Campus Box 390, Boulder, Colorado 80309-0390, USA

Scott Burdick

Department of Earth, Atmospheric, and Planetary Sciences, Massachusetts Institute of Technology, 77 Massachusetts Avenue, Cambridge, Massachusetts 02139, USA

[1] We document our tomographic method and present a new global model of three-dimensional (3-D) variations in mantle *P* wave velocity. The model is parameterized by means of rectangular cells in latitude, longitude, and radius, the size of which adapts to sampling density by short-period (1 Hz) data. The largest single data source is ISC/NEIC data reprocessed by Engdahl and coworkers, from which we use routinely picked, short-period *P*, *Pg*, *Pn*, *pP*, and *pwP* data (for earthquakes during the period 1964~2007). To improve the resolution in the lowermost and uppermost mantle, we use differential times of core phases ($PKP_{AB} - PKP_{DF}$, $PKP_{AB} - PKP_{BC}$, $P_{diff} - PKP_{DF}$) and surface-reflected waves (*PP-P*). The low-frequency differential times (P_{diff}, *PP*) are measured by waveform cross correlation. Approximate 3-D finite frequency kernels are used to integrate the long-period data (P_{diff}, *PP*) and short-period (*P*, *pP*, *PKP*) data. This global data set is augmented with data from regional catalogs and temporary seismic arrays. A crust correction is implemented to mitigate crustal smearing into the upper mantle. We invert the data for 3-D variations in *P* wave speed and effects of hypocenter mislocation subject to norm and gradient regularization. Spatial resolution is ~100 km in the best sampled upper mantle regions. Our model, which is available online and which will be updated periodically, reveals in unprecedented detail the rich variation in style of subduction of lithospheric slabs into the mantle. The images confirm the structural complexity of downwellings in the transition zone discussed in previous papers and show with more clarity the structure of slab fragments stagnant in the transition zone beneath east Asia. They also reveal low wave speed beneath major hot spots, such as Iceland, Afar, and Hawaii, but details of these structures are not well resolved by the data used.

Components: 8797 words, 14 figures, 1 table.

Keywords: seismic tomography; mantle; traveltimes; *P* wave speed.

Index Terms: 6982 Radio Science: Tomography and imaging (7270, 8180); 7208 Seismology: Mantle (1212, 1213, 8124); 7203 Seismology: Body waves.

1. Introduction

[2] With ever increasing quantity and quality of seismic data from global and (permanent and temporary) regional seismograph networks, global tomography has been providing increasingly detailed constraints on mantle structure and convection (see reviews by, e.g., *Dziewonski and Woodhouse* [1987], *Masters* [1989], *Montagner* [1994], *Dziewonski* [1996], *Kárason and van der Hilst* [2000], *Fukao et al.* [2001], and *Trampert and van der Hilst* [2005]). Although increasingly consistent spatial patterns of wave speed variations on the large scale have emerged, at length scales less than ~1000 km conspicuous discrepancies still exist. These differences limit our understanding of large-scale geological processes. The need of high-quality tomographic models continues to drive the improvement both in data coverage and in theoretical and computational aspects of wave propagation and inversion.

[3] In the past decade we have been updating our global *P* wave models in response to the availability of new data sets or better methodologies for data processing and inversion. These models have been made available to and used by the community. The main objectives of this paper are twofold. First, we document the procedures currently used in our global tomography. Second, we present (and make available) a new global *P* wave model, which is an update of the model presented by *Kárason and van der Hilst* [2001].

[4] Our regional [e.g., *van der Hilst et al.*, 1991; *van der Hilst*, 1995; *Widiyantoro and van der Hilst*, 1996; *Li et al.*, 2006] and global [e.g., *van der Hilst et al.*, 1997; *Kárason and van der Hilst*, 2001] tomography has evolved over time, but the key aspects can be summarized as follows. First, to maximize the effective sampling of Earth's interior structure we use carefully processed (and integrated) data from a wide range of seismic phases (e.g., *P*, *Pg*, *PP*, *pP*, *PKP*, *Pdiff*). Second, where possible we augment existing data sets with new data from regional networks and temporary seismic arrays [*Li et al.*, 2006; C. Li et al., Subduction of the Indian lithosphere beneath the Tibetan Plateau and Burma,

submitted to *Earth and Planetary Science Letters*, 2008]. Third, we use (approximate) 3-D sensitivity kernels to allow long-period data to constrain long-wavelength wave speed variations without preventing short-period data from resolving smaller-scale structures [e.g., *Kárason and van der Hilst*, 2001]. Fourth, we use an irregular parameterization to enhance resolution in regions of dense data coverage or special interest [*Kárason and van der Hilst*, 2000]. Finally, we use a crust correction to mitigate imaging artifacts due to crustal heterogeneity that is not resolved by the data used [*Li et al.*, 2006].

[5] The combined use of finite frequency sensitivity kernels and adaptive parameterization makes it possible to resolve structure at a range of length scales. Indeed, regionally our model constrains heterogeneity in much more detail than can be appreciated from global maps. As an example of this multiscale aspect of our global model, Figure 1b shows a zoom-in of the global model (depicted in Figure 1a) to illustrate structure at 100 km depth beneath the eastern Tibetan Plateau and southwestern China whereas Figure 1c depicts slabs of subducted lithosphere under South America.

[6] In section 2, below, we describe the data selection and processing that underlie our tomography. Subsequently, in section 3 we document the technical aspects of our method, including the construction of the sensitivity matrix (and a brief discussion of the issue of finite frequency sensitivity kernels), the use of irregular parameterization, and the crust correction. In sections 4 and 5 we present a new model and discuss some of the first-order features.

2. Data

[7] We use traveltime residuals with respect to times computed from *ak135* [*Kennett et al.*, 1995], a spherically symmetric reference model for *P* wave speed. We use 3 types of data (Table 1): (1) routinely picked and processed traveltimes from global and regional networks; (2) differential times measured by waveform
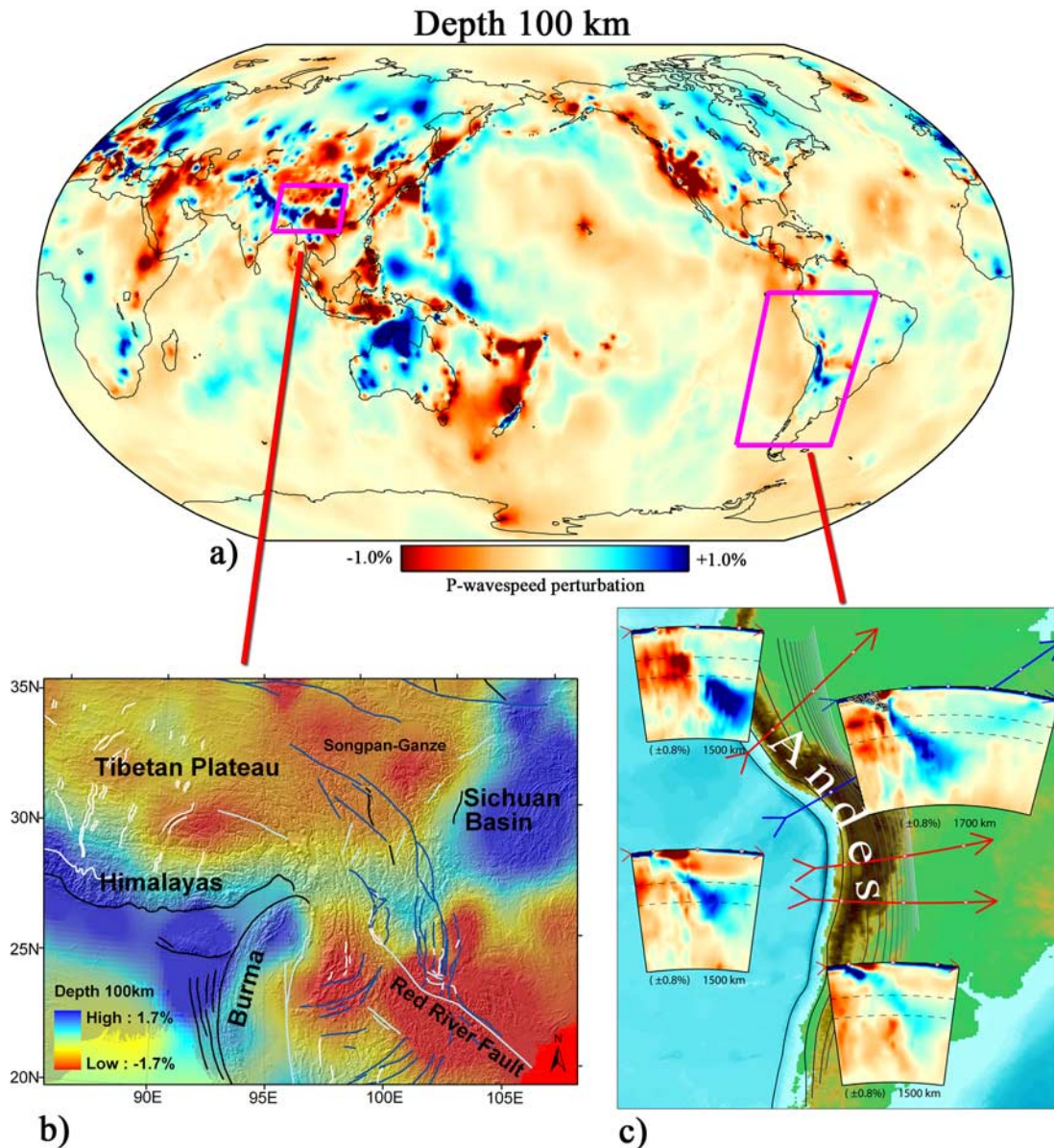
Figure 1. Multiscale global tomography. (a) Global *P* wave speed variations at 100 km depth. (b) Regional wave speed heterogeneity at 100 km in eastern Tibetan plateau and SW China with topography and major active faults, where black, white, blue, and gray lines represent thrust, normal, left strike-slip, and right strike-slip faults, respectively. (c) Four cross sections through the Andean subduction zone under South America. The dashed lines on images represent 410 km and 660 km discontinuities. Gray circles in the blue arrow cross section show earthquakes.

cross correlation; and (3) phases arrivals from temporary arrays.

2.1. Routinely Processed Traveltimes

[8] The largest single source of routinely processed global data used is the database of traveltime residuals maintained by E. R. Engdahl and co-workers [*Engdahl et al.*, 1998] (hereinafter referred to as the EHB data). This data results from rigorous reprocessing of arrival times reported to the International Seismological Centre (ISC) and the U.S. Geological Survey's National Earthquake Information Center (NEIC), including nonlinear earthquake re-location and phase re-identification. The global data coverage by the EHB is augmented by data from regional networks and temporary arrays that

Table 1. Data Sources for Global Tomography[a]

Phases	Number of Records	Number of Comp. Ray	Frequency	Kernel	Source
P	10.3×10^6	3.0×10^6	1 Hz	Rays	EHB
Pn	1.3×10^6	2.0×10^5	1 Hz	Rays	EHB
Pg	1.8×10^6	4.1×10^4	1 Hz	Rays	EHB
pP and *pwP*	7.1×10^5	3.9×10^5	1 Hz	Rays	EHB
PKP_{AB}-$PKP_{DF/BC}$	2.4×10^5	9.6×10^4	1 Hz	Rays	EHB
PKP_{AB}-$PKP_{DF/BC}$	1,383	N/A	1 Hz	Rays	McSweeney
PKP_{diff}-PKP_{DF}	543	N/A	50 mHz	3-D	Wysession
PP-P	20,266	N/A	40 mHz	3-D	Masters
P	8.1×10^5	3.5×10^5	1 Hz	Rays	CSN+Array
Pn	6,600	3,300	1 Hz	Rays	CSN+Array

[a] EHB, *Engdahl et al.* [1998]; McSweeney, *McSweeney* [1995]; Wysession, *Wysession* [1996]; Masters, *Bolton and Masters* [2001]; CSN, Chinese Seismograph Network; Array, arrays in Tibet, Australia, USA, and Africa. Ray geometry is depicted in Figure 2 (comp. ray, composite rays).

do not report to the ISC or NEIC. Figure 3a shows the global distribution of stations contributed to the combined data set.

[9] The EHB data is regularly updated and previous versions have been used in regional [e.g., *van der Hilst et al.*, 1991; *Li et al.*, 2006] and global studies [e.g., *van der Hilst et al.*, 1997; *Bijwaard et al.*, 1998; *Boschi and Dziewonski*, 1999; *Kárason and van der Hilst*, 2000, 2001; *Zhao*, 2004; *Montelli et al.*, 2004, 2006a]. The EHB data used here comprises more than ten million traveltime residuals associated with more than 450,000 well constrained regional and teleseismic earthquakes from

1964 to 2007 (Table 1 and Figure 2). We use *P*, *pP* and *pwP* [e.g., *van der Hilst et al.*, 1991; *van der Hilst and Engdahl*, 1991; *van der Hilst et al.*, 1997], *PKP* [*Kárason and van der Hilst*, 2001], and (for the first time) *Pg* and *Pn*. The phase *Pg* propagates in the crust and gives more constraints on shallow structure. In the EHB catalog, *P* phases with turning points less than 410 km are labeled "*Pn*." In order to select turning rays and omit the post-critical "head wave" we use phases labeled "*Pn*" as turning *P* waves if the focal depths are larger than 80 km or if the turning points are larger than 100 km depth. The depth phase *pP* bounces off Earth's surface and *pwP* propagates through
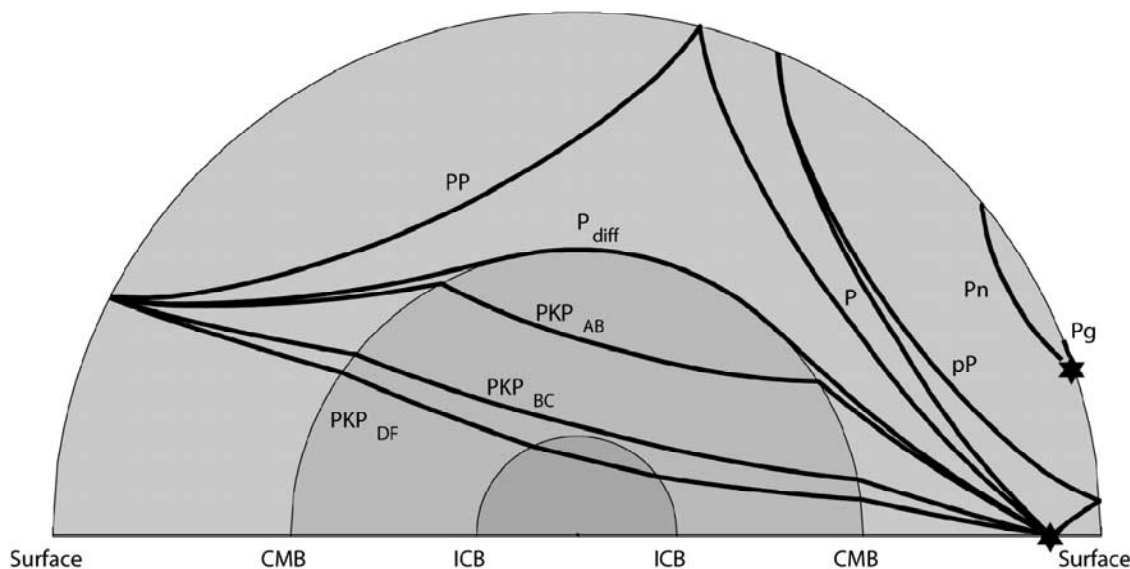

Figure 2. The raypaths of the phases used in this study. Black stars represent sources. "*P*" is the direct compression wave and does not travel through the core. "*pP*" is upgoing from the source, while "*PP*" is downgoing; both bounce once off the Earth's surface. "*Pg*" propagates in the crust. We define "*Pn*" as having a focal depth larger than 80 km or a turning point deeper than 100 km in the EHB data. "PKP_{AB}" and "PKP_{BC}" travel through the outer core, while "PKP_{DF}" travels through both the outer and inner cores and "*Pdiff*" grazes the core.
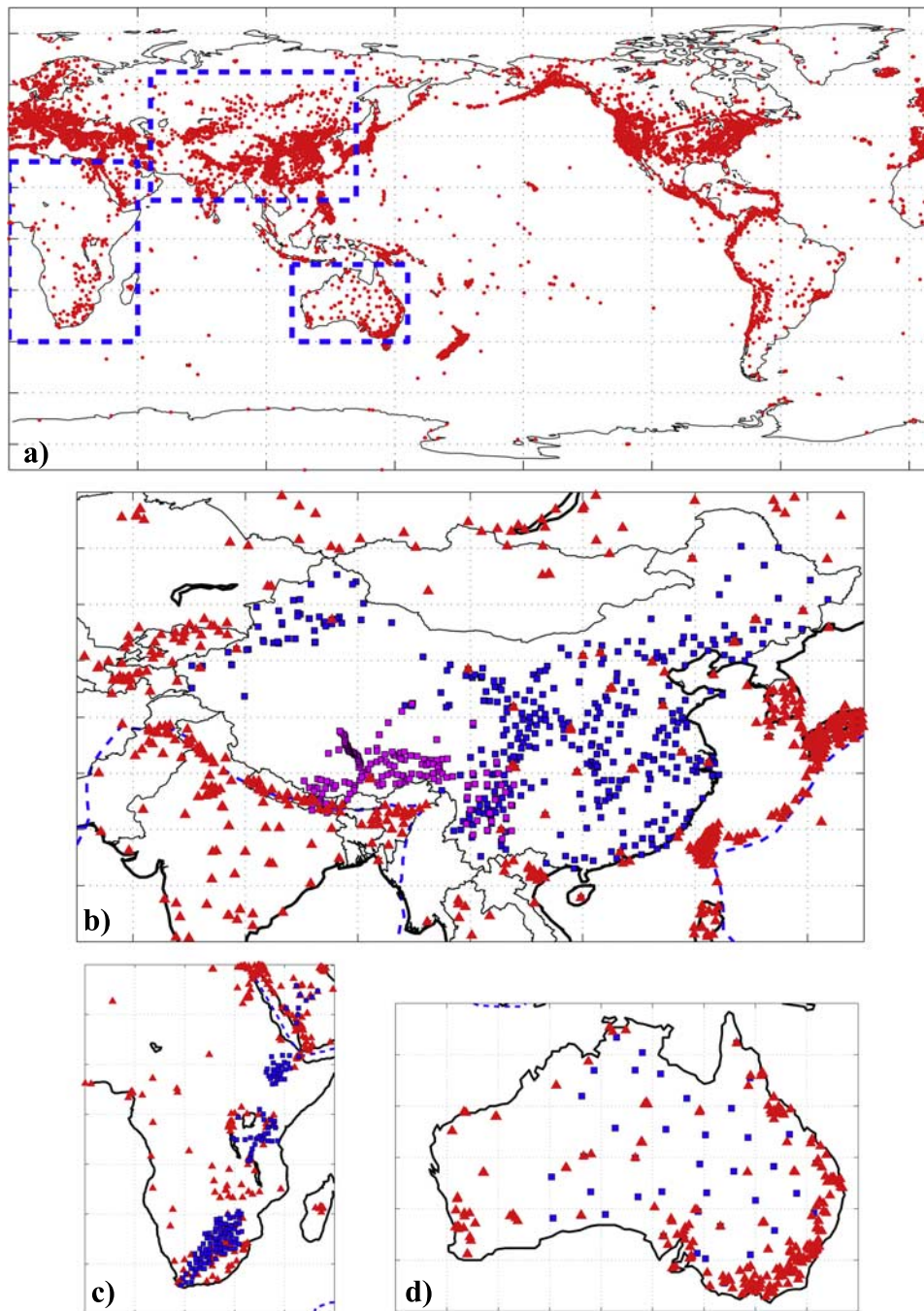
Figure 3. (a) Global station distribution of the combined database (red dots). The dashed blue rectangles represent zoom-in regions in the following subplots. (b) Stations of Tibetan arrays (magenta squares) and Chinese (including Kyrgyzstan) Seismograph Network (blue squares) are complimentary to EHB stations (red triangles) in east Asia. (c) Station additions from African arrays (blue squares). (d) Station additions from the SKIPPY project (blue squares) in Australia.

water and bounces off the surface of the ocean. The traveltime residuals for these phases are corrected for topography and bathymetry (water depth), respectively. Following *Kárason and van der Hilst* [2001] we use the EHB *PKP* data for stations that

have two or more *PKP* arrivals so that the construction of differential times ($PKP_{AB} - PKP_{DF}$ or $PKP_{AB} - PKP_{BC}$) is possible. This appears to be a good quality control because multiple *PKP* arrivals can only be seen on high-quality records. As a

down side, a large fraction of the available EHB*PKP* data is not used (e.g., *PKP*$_{DF}$ for $\Delta >$ 150°). The *PKP*$_{DF}$ data (in *PKP*$_{AB}$ − *PKP*$_{DF}$) is corrected for inner core heterogeneity and anisotropy according to *Su and Dziewonski* [1995], but the mantle model is rather insensitive to this effect.

[10] In addition to the EHB data we also use routinely processed traveltime picks from the Annual Bulletin of Chinese Earthquakes and from stations of the Chinese Seismograph Network [e.g., *Li et al.*, 2006; Li et al., submitted manuscript, 2008], which produces a large amount of data at stations not represented in the ISC catalog (Figure 3b). Incorporation of data from different catalogs requires significant care. After carefully removing repetition of data from stations reporting to multiple data centers, we process this part data along with the EHB data in order to correct for base line inconsistencies that can result from using different reference models and hypocenter location algorithms.

[11] The ray coverage could be improved further by including routinely processed traveltime data from other later arriving phases, such as *PP* and *PcP*. *Van der Hilst and Engdahl* [1991] and *Kárason and van der Hilst* [2001] found that EHB*PP* and *PcP*, respectively, are rather noisy. While checkerboard tests would indicate improved resolution resulting from the addition of raypaths it is not obvious that these phase data improve the actual tomographic model. For this reason, we do not use routinely processed (short-period) traveltime picks of *PcP* and *PP*.

2.2. Waveform-Based Differential Times

[12] To complement the data set of routinely processed picks, we also used high-frequency *PKP* differential traveltimes [*McSweeney*, 1995] measured by cross correlation of the observed *PKP* waveform with a synthetic signal calculated from theoretical predictions. To improve the sampling of deep mantle structures further, our tomography also uses *PKP*$_{DF}$ − *P*$_{diff}$ differential times [*Kárason and van der Hilst*, 2001]. The *P*$_{diff}$ phases are diffracted along the core-mantle boundary (CMB) and their differential traveltime residuals are sensitive to structure near the base of the mantle. These data are measured at relatively low frequency (central frequency ∼0.05 Hz) by *Wysession* [1996].

[13] Finally, to increase our ability to resolve structures in the upper mantle of intraplate regions with few earthquakes and stations, we use long-period *PP-P* data, measured at a frequency ∼0.04 Hz [*Bolton and Masters*, 2001]. The measurement is made by cross-correlating the Hilbert transform of *P* arrival with the *PP* arrival while accounting for attenuation [*Woodward and Masters*, 1991].

[14] We refer to *Kárason and van der Hilst* [2001] for more information about the processing of these differential time data and their integration with the routinely processed arrival time picks described above.

2.3. Temporary Arrays

[15] Data from temporary arrays is not usually reported to the ISC or NEIC but has much potential for improving resolving the upper mantle structure because such arrays are typically deployed in regions where permanent sites are few and far between. For example, we have added data from the temporary arrays in Australia [*van der Hilst et al.*, 1994], on the Tibetan plateau and SW China [*Li et al.*, 2006; Li et al., submitted manuscript, 2008], and in Africa [*Benoit et al.*, 2006]. These data are corrected for elevation and Earth's ellipticity and processed along with the EHB data. Furthermore, we have begun to incorporate traveltime data from seismograph stations of the USArray [*Burdick et al.*, 2008].

3. Methodology

[16] For our global tomography we use an iterative least squares method (LSQR) [*Paige and Saunders*, 1982; *Nolet*, 1985] to minimize the following cost function:

$$\varepsilon = \|Am - d\|^2 + k_1\|Lm\|^2 + k_2\|m\|^2 + k_3\|C - M_C\|^2$$

Here, *A* is the sensitivity matrix, *m* is the model vector, *d* is the data vector, *L* is a smoothing operator, *C* and *M*$_C$ are matrices associated with the crust correction (see below), and k$_i$ control the weights of the three regularization terms relative to the first term on the right-hand side (r.h.s.), which represents the control by the data. The model *m* includes not only the wave speed perturbations (in non-overlapping and constant-slowness blocks) relative to *ak135* [*Kennett et al.*, 1995] but also the parameters associated with hypocenter mislocation [e.g., *Spakman and Nolet*, 1988]. In order to deal with noisy data and possible singularity in the inversion we use regularization. The gradient damping (second term on r.h.s.) smoothes the

model and the norm damping (third term on r.h.s.) seeks to find the best model with small variations from the reference model. The results presented here were obtained after 200 iterations, although for LSQR most of the convergence is achieved within a small number of iterations.

3.1. Raypaths and 3-D Sensitivity Kernels

[17] The center frequency of the short-period traveltime data is ~1 Hz, and for the linearized tomographic inversion we back-project these data along raypaths calculated in the one dimensional (1-D) *ak135* reference model for mantle *P* wave speed. For the (expanded) EHB data, we use weighted composite rays to reduce the size of the sensitivity matrix [e.g., *Spakman and Nolet*, 1988].

[18] The use of infinitesimally narrow rays is, strictly speaking, not appropriate for the long-period data measured by waveform cross correlation, such as the differential traveltimes P_{diff}–PKP_{DF} and *PP-P* used here. Following *Kárason and van der Hilst* [2001] and *Kárason* [2002], for these data we use approximate 3-D sensitivity kernels. The use of such kernels is attractive in that they allow the distribution of sensitivity of low-frequency data to structural heterogeneity over more realistic mantle volumes than infinitesimally narrow rays. Effectively, it allows the low-frequency data to constrain large-scale variations in structure without degrading the resolution in regions of dense sampling by high-frequency data. To balance the small, but high-quality waveform data sets against the much larger, but noisier EHB data, we give them extra weight [*Kárason and van der Hilst*, 2001].

[19] For inversion of broadband waveforms, with a range of (frequency) scales in the data, the use of full wave kernels is important [*de Hoop and van der Hilst*, 2005a; *de Hoop et al.*, 2006; *Tromp et al.*, 2005], but for tomography with traveltime residuals based on a single-step linearization (with kernels calculated in a quasi-homogeneous background) simple approximations are adequate [*Dahlen et al.*, 2000; *Kárason*, 2002].

[20] For computational efficiency, we calculate approximate kernels by exploiting the intrinsic symmetry of kernels (in homogeneous, but depth-dependent media) and, in some cases, by interpolation between exact kernels calculated at a small number of epicentral distances. For example, for the incorporation of evanescent core-diffracted P_{diff} waves, *Kárason and van der Hilst* [2001] infer
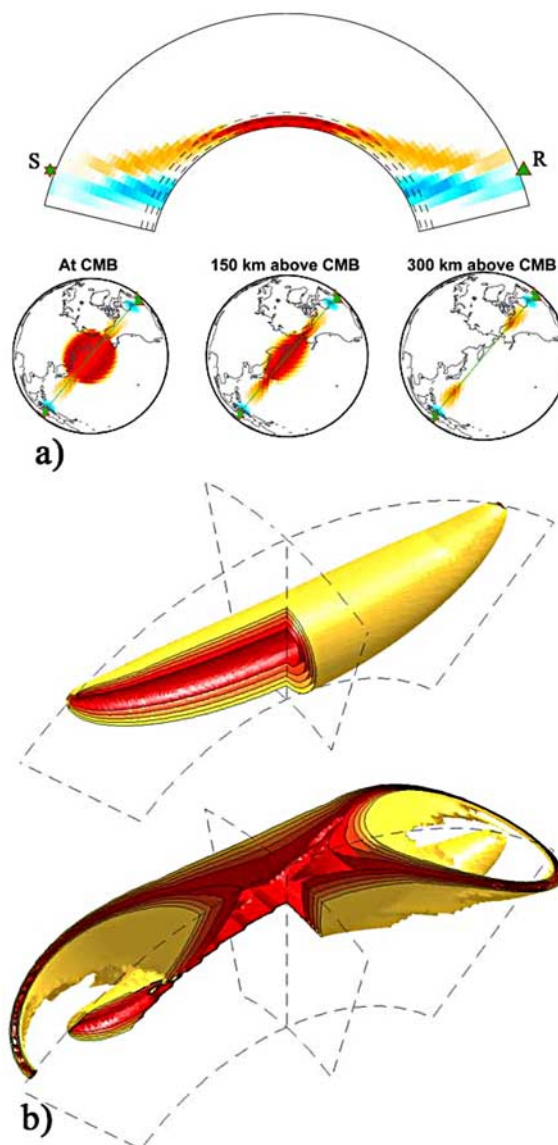

Figure 4. Three-dimensional finite frequency kernels [after *Kárason*, 2002]. (a) Sensitivity to slowness variations within the Earth for low-frequency $PKP_{DF} - Pdiff$ differential times. Red and blue indicate negative and positive sensitivities, calculated by subtracting *Pdiff* from PKP_{DF}. (b) Surfaces representing constant traveltime deviations, using single scattering for *P* and *PP*, respectively. One quadrant is cut out to see the interior of the 3-D kernels. Redder colors correspond to smaller traveltime deviations. We assume zero sensitivity outside of the yellow surface, which represents the first Fresnel zone.

simple kernels from exact results of mode summation [*Zhao and Jordan*, 1998; *Zhao et al.*, 2000]. The resulting kernels distribute sensitivity over a large irregularly shaped volume (Figure 4a).

[21] For the low-frequency *PP-P* differential times, we follow *Kárason* [2002] and use single scattering theory to estimate 3-D kernels, neglecting the sensitivity to structure outside the first Fresnel zone. Figure 4b depicts the absolute traveltime surfaces for *P* and *PP*, respectively. The yellow surface represents the first Fresnel zone calculated from the dominant frequency of the *PP-P* data. The differential *PP-P* kernel is obtained by subtracting the *P* from the *PP* kernel [*van der Hilst and Engdahl*, 1991].

3.2. Sensitivity Matrix *A*: Adaptive Parameterization

[22] We parameterize the tomographic model by means of local basis functions consisting of non-overlapping and constant-slowness cells [*Spakman and Nolet*, 1988]. The part of the sensitivity matrix *A* associated with short-period data then consists of the total length of the rays traversing such cells whereas the part of *A* associated with the low-frequency data is obtained through projection of the 3-D kernels onto such basis.

[23] The uneven sampling of mantle structures by seismic waves results in significant lateral variations in resolution. The use of a regular grid would either over-parameterize poorly sampled regions (also be computationally inefficient) or average out small-scale structures. Local basis functions can, however, be adjusted to the expected resolution [e.g., *Abers and Roecker*, 1991; *Fukao et al.*, 1992; *Widiyantoro and van der Hilst*, 1996; *Bijwaard et al.*, 1998]. We follow *Kárason and van der Hilst* [2000] and construct an adaptive parameterization scheme on the basis of sampling density (hit counts) of the short-period data. In this algorithm, the adaptive grid is constructed by combining one or more cells from the base grid to reach a minimum ray density in each cell (we use a minimum hit count of 900). The base grid is approximately 0.7° in latitude and longitude and 45 km in depth throughout the mantle. With increasing depth, the minimum cell size increases in accordance with the increasing width of the Fresnel zones of short-period *P* waves. The total number of cells used in the inversion, that is the length of model vector *m*, is ~500,000.

3.3. Crust Correction

[24] The small incidence angles of teleseismic *P* waves may map unresolved crustal heterogeneity to greater depths in the mantle. One can correct the data explicitly for the contribution (to the travel-times) of propagation through the crust. This is, however, sensitive to error in the crust model and may result in introducing as many artifacts as one wants to remove. Instead, we correct for crustal structure by means of regularization to (that is, forcing the solution toward) an a priori 3-D crustal model [*Li et al.*, 2006]. In addition to the simplicity of implementation, the correction through regularization in the model space can balance the crust and upper mantle contribution to a misfit (through the weight k_3 in the penalty function). Furthermore, later addition of data, the use of data with complex sensitivity to shallow structure, such as the minimax *PP* phase, or updates of the reference crust model do not require further calculation other than re-running the inversion. We use CRUST 2.0 [*Bassin et al.*, 2000] as the a priori global reference and embed higher-resolution regional models where available.

3.4. Regularization (Damping)

[25] As in our previous studies, we regularize the inversion using a combination of norm damping, which tends to minimize the amplitude of the model, and gradient damping, which produces smooth variations, both laterally and radially. We perform experiments with synthetic data from known input models to find appropriate values for the damping parameters (that is, k_1 and k_2 in the cost function), but the choice of these parameters is subjective. We prefer small values for the norm damping and for the gradient damping in the radial direction.

4. Results

[26] The results of checkerboard tests give (qualitative) insight into the general resolution of our global model (Figure 5). The input pattern has a half wavelength of ~5° and the constant amplitude of 1.5% in the upper half of the mantle. In the lower half of the mantle, the half wavelength is ~10°. In this way the half wavelength of input pattern is similar (~550 km) near Earth's surface and at the base of the mantle. The input anomalies were put at one depth at a time. Noiseless synthetic traveltimes were created and inverted using the same inversion scheme as for the observed data. Although the resolution is still spatially variable in the upper mantle due to the uneven distribution of stations and zones of active seismicity, and generally poor beneath the southern hemisphere, we are continually improving the ability to recover mantle structure by adding new data sets (Figures 3b–3d).
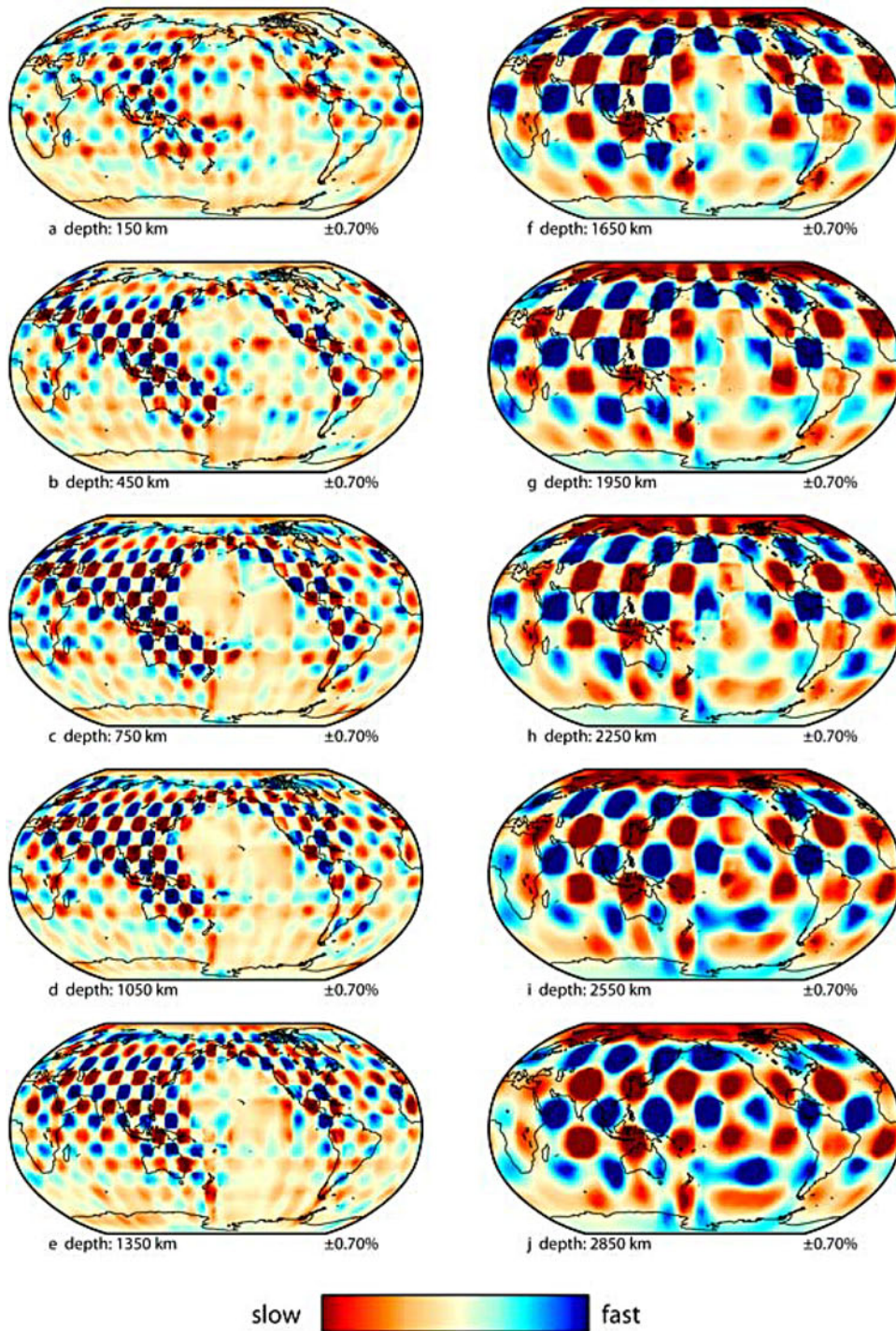
Figure 5. Recovery fields of global resolution tests, using harmonic input patterns with constant amplitude ±1.5% in wave speed throughout the mantle. (a–e) Half-wavelength of ~5° (spatial wavelength of ~550 km at the surface). (f–j) Half-wavelength of ~10° (~600 km at the CMB).

The amplitude recovery is spatially variable but generally less than 70%, in part because of the damping that we use to suppress the effects of noise in the data.

[27] Our new model for *P* wave speed variations is hereinafter referred to as MIT-P08. Figure 6 depicts *P* wave speed variations at selected mantle depths, in which the color bar is adapted to the radial

changes in strength of the anomalies. To appreciate the change in surface area with depth, Figure 7 displays resolution and wave speed maps with an appropriate scaling of the surface area (and with the same color bar throughout). MIT-P08 is generally consistent with our earlier models [e.g., *van der Hilst et al.*, 1997; *Kárason and van der Hilst*, 2000, 2001] but locally it shows more detail. A comprehensive discussion of MIT-P08 is beyond the scope of this paper, but we illustrate its multi-scale aspects with examples pertinent to upper mantle structure, slabs of subducted lithosphere, and mantle upwellings.

4.1. Upper Mantle Structure

[28] At long wavelengths, slow back arc regions, fast subduction zones, and fast craton signatures are prominent in the map views of upper mantle structure (Figure 6a), but in many regions the data resolves structure on much smaller scales than can be appreciated from the global perspective. As an illustration of the high resolution in regions of dense data coverage (Figure 3b), Figure 8a depicts the shallow structure beneath east Asia. The incorporation of data from the Chinese Seismological Network and from temporary arrays in Tibet produced a significant increase in resolution of upper mantle structure (auxiliary material[1] Figure S1). Tomographically inferred mantle heterogeneity correlates well with geological features [*Li et al.*, 2006; Li et al., submitted manuscript, 2008]. For example, the high-velocity anomalies beneath the Himalayas and the southwestern margin of the Tibetan Plateau probably mark subducted Indian lithosphere, and the Precambrian Sichuan and Ordos basins are marked by fast anomalies.

[29] In accord with regional and global surface wave studies, MIT-P08 reveals slow wave propagation in the upper mantle beneath the western part of North America and seismically fast continental lithosphere beneath the Great Plains and the Canadian Shield (Figure 8b). Resolution in the upper mantle beneath North America is not yet as good as beneath east Asia, but addition of *USArray* data will change this in the years to come [*Burdick et al.*, 2008].

4.2. Slabs of Subducted Lithosphere

[30] As in our previous models [*van der Hilst et al.*, 1997; *Kárason and van der Hilst*, 2000, 2001],

the presumed slabs of subducted lithosphere are generally well resolved in MIT-P08. Indeed, long and narrow traces of fast materials from the upper mantle transition zone to mid-mantle depths are visible beneath North and South America and southern Asia (Figures 6b–6f). These structures have previously been associated with plate motion history and are thought to be the remnants of old subducted slabs. We illustrate the detail in MIT-P08 by means of vertical sections across three major convergent plate boundaries (Figures 9–11).

[31] Sections 1–3 in Figure 9 show complex upper mantle structures associated with the subduction of the Cocos plate along the Middle America trench [see also *van der Hilst*, 1990], whereas sections 4 and 5 give insight into the subduction of the Atlantic lithosphere into the transition zone beneath the Lesser Antilles arc and the deep subduction of the Farallon plate beneath the Caribbean plate [see also *van der Hilst and Spakman*, 1989; *van der Hilst et al.*, 1997; *Grand et al.*, 1997; *Ren et al.*, 2007]. Sections 6–9 illustrate variations in the style of subduction of the Nazca and Farallon plates beneath South America (for detailed discussions of these structures and the tectonics we refer to our regional studies [e.g., *van der Hilst and Mann*, 1994; *Engdahl et al.*, 1995; *Ren et al.*, 2007]). The spatial resolution decreases southward along the arc as a result of the (general) degradation of data coverage in the southern hemisphere, and the structure associated with westward subduction beneath the South Sandwich Islands only barely stands out above the background (section 10).

[32] Figure 10 illustrates mantle structures associated with subduction of oceanic lithosphere beneath the western Pacific island arcs, from Kamchatka in the north, along the Kuril Islands and Japan, to Izu Bonin and Mariana in the south. As was observed previously [e.g., *van der Hilst et al.*, 1991; *Fukao et al.*, 1992; *van der Hilst and Seno*, 1993; *Fukao et al.*, 2001; *Miller et al.*, 2004], the style of seismicity and subduction varies dramatically along these trenches. In the north, the slab is rather steep and connects to lower mantle structures, and its seismic Wadati-Benioff zone reaches well into the transition zone (sections 11, 12). Southward, the dip angle gradually decreases to ~30° below central Japan and large aseismic parts of the slabs appear stagnant in the transition zone beneath eastern China (sections 13, 15, and 16). Section 16 reveals the complex transition zone structure associated with the subduction of Pacific
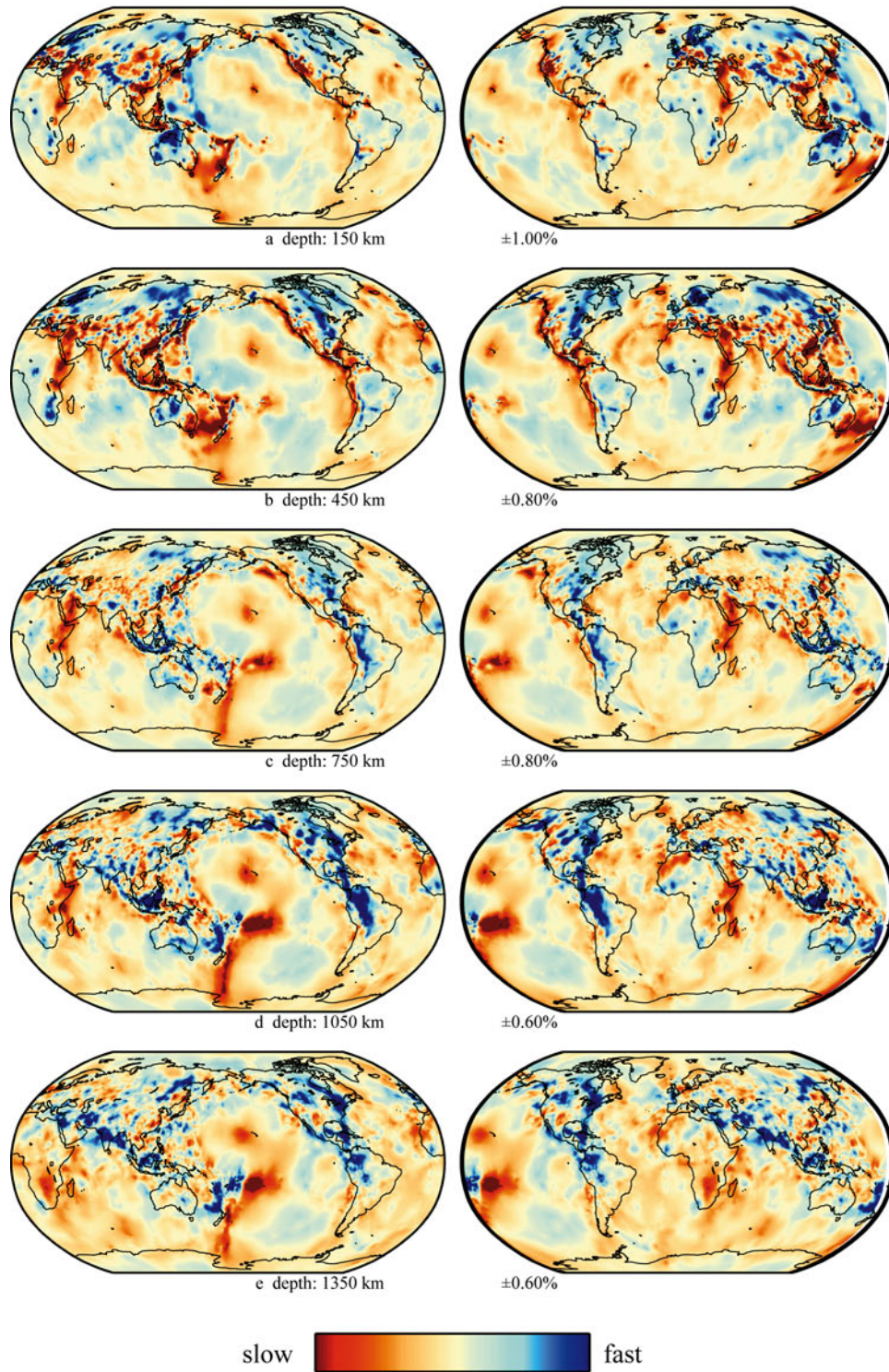
Figure 6. Global *P* wave speed heterogeneity at several selected depths using the Robinson projection centered (left) on the Pacific Ocean and (right) on Africa.
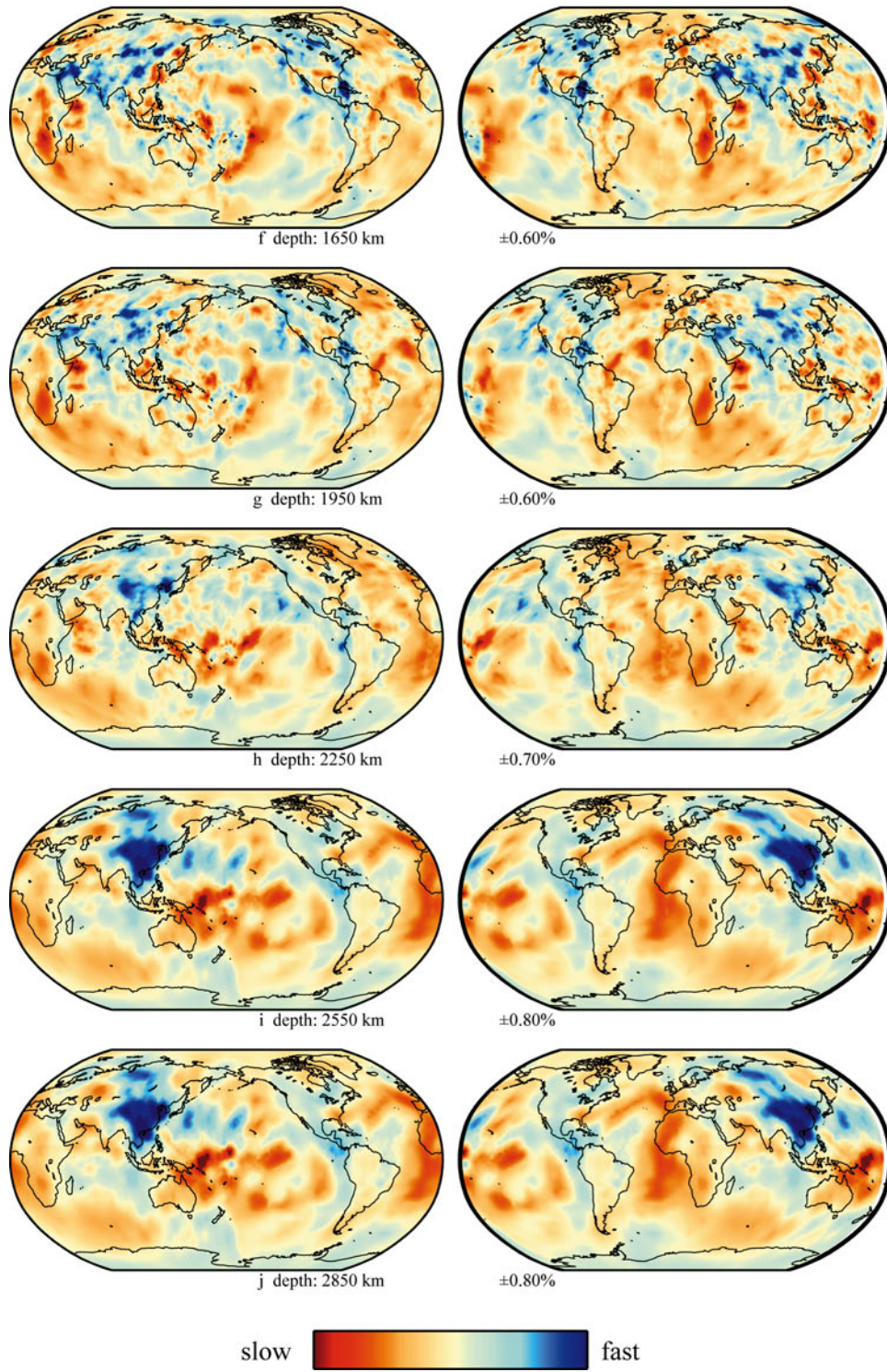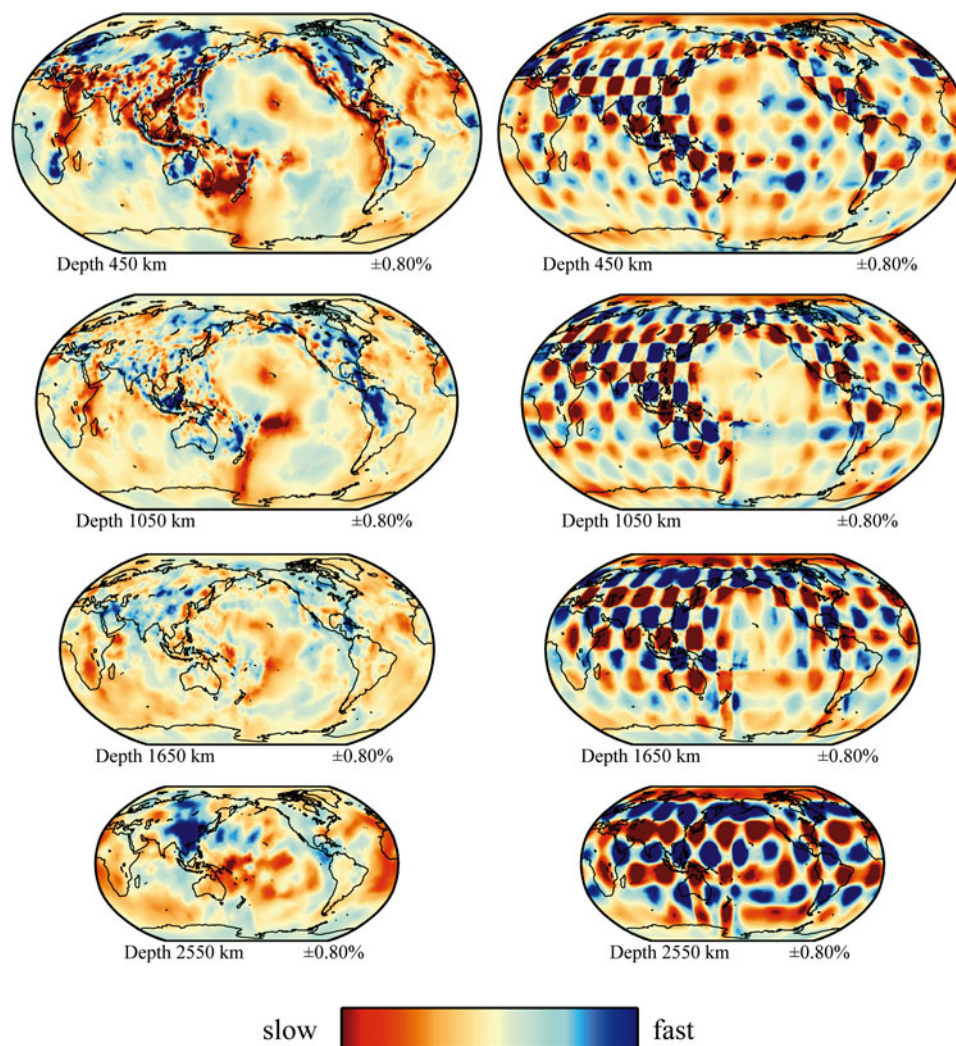
f depth: 1650 km   ±0.60%

g depth: 1950 km   ±0.60%

h depth: 2250 km   ±0.70%

i depth: 2550 km   ±0.80%

j depth: 2850 km   ±0.80%

slow ────────── fast

Figure 6. (continued)

Depth 450 km ±0.80%   Depth 450 km ±0.80%

Depth 1050 km ±0.80%   Depth 1050 km ±0.80%

Depth 1650 km ±0.80%   Depth 1650 km ±0.80%

Depth 2550 km ±0.80%   Depth 2550 km ±0.80%

slow   fast

Figure 7. The scale effect with radius both for the model (with the same color scale, ±0.8%) and checkerboard test.

and Philippine Sea plates at the Izu Bonin and Ryukyu trenches, respectively, and section 17 shows that beneath the Mariana Trench a slab seems to sink directly into the lower mantle. The new images of the lateral variation along the Izu Bonin and Mariana subduction systems are in agreement with *van der Hilst and Seno* [1993], and later studies such as *Miller et al.* [2004], but owing to the added data coverage in SE Asia the structure of the stagnant parts beneath the northern part of the Philippine Sea plate and SE Asia is being revealed with increasing clarity (e.g., section 16).

[33] Figure 11 illustrates structures associated with the subduction of the Indo-Australia and Pacific plates beneath Indochina [see also *Widiyantoro and van der Hilst*, 1996; *Replumaz et al.*, 2004;

Hafkenscheid et al., 2001, 2006]. The subducted slabs beneath the Celebes Sea (section 21) and the Philippine trench (section 22) are clearly defined and reach into the lower mantle. Subduction of the Indian plate beneath the Sunda arc is continuous to at least 1,600 km depth (sections 19, 20). The images also reveal a large, seismically fast structure in the lower mantle (section 21, 22), which we interpret as a deep accumulation of slab fragments that subducted along the Sunda arc from the south and the Banda, Halmahera, and Philippine trenches from the east.

4.3. Upwellings

[34] We have not added data sets that specifically improve the sampling of the mantle beneath "hot spots" in oceanic intra plate regions. Therefore,
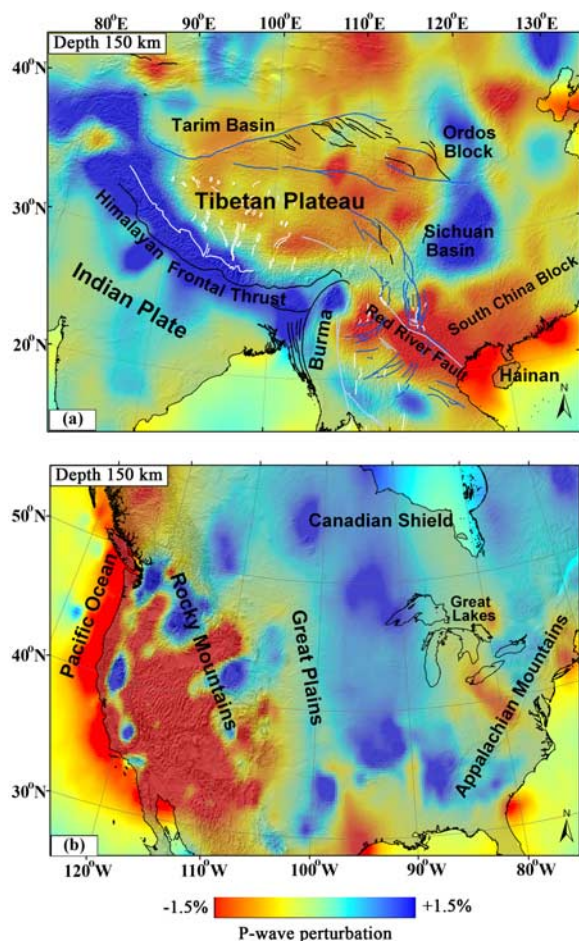
Figure 8. The continental (upper mantle) structure of (a) east Asia and (b) North America at 150 km depth [see also *Burdick et al.*, 2008].

apart from a general improvement in resolution, our current model is in this regard not much different from our previous models. Instead of producing a "catalog of deep mantle plume" [*Montelli et al.*, 2006a] we point out the most conspicuous anomalies. We use "hot spots" [*Courtillot et al.*, 2003] for geographical reference.

[35] In the upper mantle and transition zone (Figures 6a and 6b), the most pronounced low wave speed anomalies are associated with back arc regions of the circum-Pacific subduction zones, with more localized regions beneath hot spots (e.g., Iceland, Hawaii, Azores, Afar, Erebus, and the Samao-Tahiti-Society Islands group) and rift zones (e.g., East Africa) with the regions of recent tectonic activity along the west coast of North America, and with Tibet. In the top 400 km of the lower mantle the slow anomalies that are most conspicuous in the global maps (Figures 6c and 6d)

are East Africa (including Afar and Lake Victoria), NW Africa (incl. Cape Verde, Canary Islands), the Azores, Hawaii, and the SW Pacific. Beneath Iceland, a localized low wave speed anomaly can be discerned until a depth of at least 1000 km (Figures 6d and 12), whereas beneath Hawaii anomalously low velocities are detected to at least ∼1800 km depth (Figure 13).

[36] Between ∼1,200 and ∼2,000 km depth, pronounced low wave speed anomalies persist beneath the central Pacific, southwest Pacific (in particular, northeast of the Solomon Islands), the Cape Verde-Canary Islands-Azores group, Ascension, the northwestern corner of the Indian plate, and beneath Africa, with the focus of the latter anomaly shifted southward with respect to the shallower structure (Figure 14). Toward the base of the mantle (e.g., Figures 6h–6j) large wavelength structures begin to dominate the spectrum [e.g., *Su and Dziewonski*, 1992]. Correction for actual surface area (Figure 7) shows that the increase in spatial length scales is, however, not as large as perceived from traditional constant area presentations of such structure (Figure 6). In the lowermost mantle large, seismically slow regions exist beneath central and southwest Pacific, northwest Africa, and the south Atlantic. These observations are mostly consistent with previous studies (auxiliary material Figure S2).

5. Discussion and Concluding Remarks

[37] In this paper we document our current method of traveltime tomography and present our new model for P wave speed in Earth's mantle, MIT-P08. We will continue to update our model when new data are available in the future. The new model is available as auxiliary material DataSet S1, and updates of the model are provided through http://eapsweb.mit.edu/research/MITP08.txt.gz.

[38] While modern data sets and computational and theoretical developments are beginning to make full waveform tomography a reality, valuable information can still be gleaned from carefully measured phase arrival times, in particular in regions where such data is available from dense (permanent and/or temporary) seismograph networks. Indeed, over the years, we have been integrating such data sets with the global set of traveltime residuals maintained by Engdahl and coworkers [*Engdahl et al.*, 1998]. Consequently, traveltime tomography has been producing images of increasing clarity and detail.
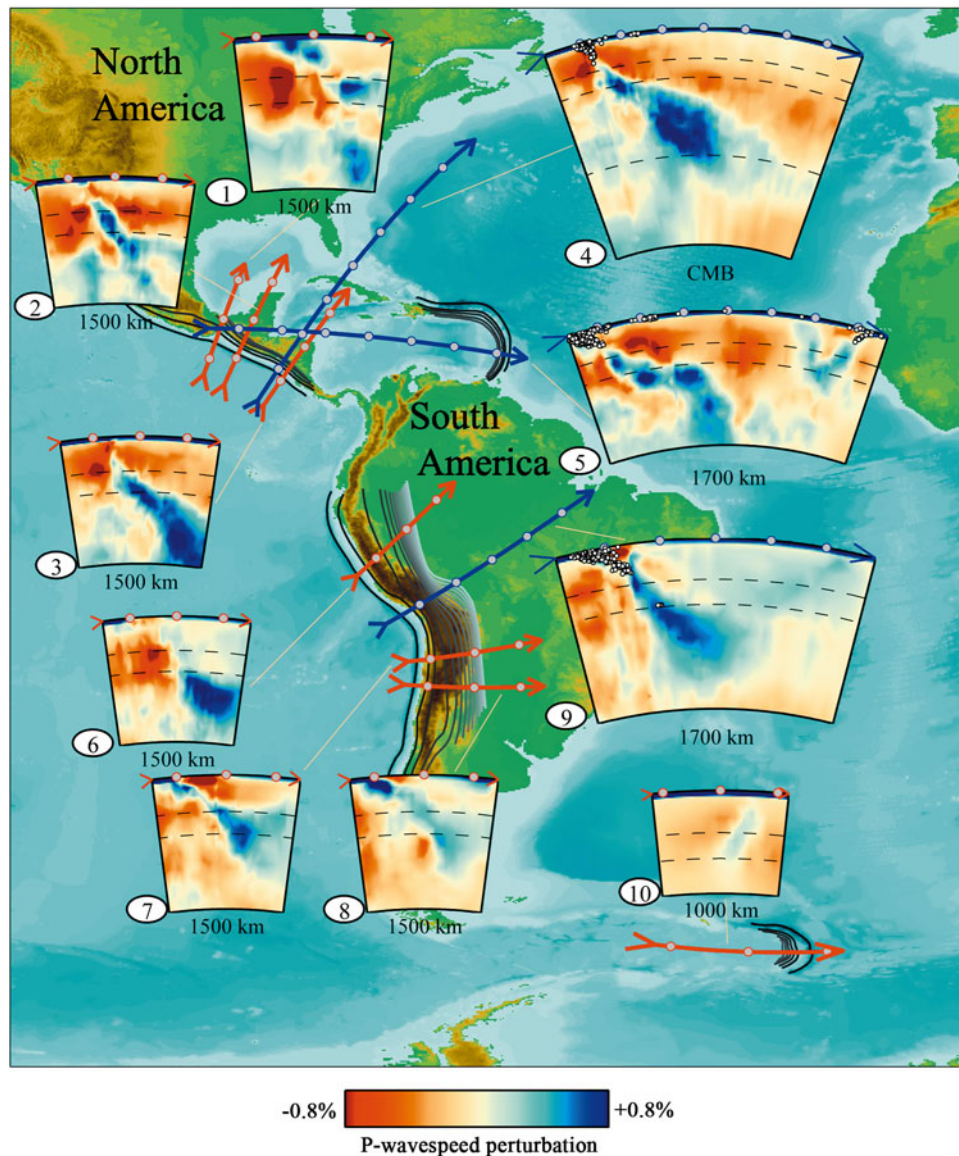
Figure 9. Subduction through Central America and South America. The gray circles on the cross sections show the earthquakes. Gray scale contours display the outline of subduction zones, as defined by slab-related seismicity [*Gudmundsson and Sambridge*, 1998].

[39] Our emphasis has been on improving data quality and quantity, but our approach to multiscale tomography has benefited from several technical changes since the construction of our first global model a decade ago [*van der Hilst et al.*, 1997]. First, we use an irregular grid to optimize resolution in regions of dense data coverage [*Bijwaard et al.*, 1998; *Kárason and van der Hilst*, 2000]. Second, we use approximate 3-D sensitivity kernels for joint inversions of data measured at different frequencies [*Kárason and van der Hilst*, 2001; *Kárason*, 2002]. Third, we use a crust correction to mitigate artifacts due to strong het-

erogeneity in the crust that cannot be resolved by the data used [*Li et al.*, 2006].

[40] We do not want to repeat the discussion in the series of comments and replies that followed *de Hoop and van der Hilst* [2005a] [see *Dahlen and Nolet*, 2005; *de Hoop and van der Hilst*, 2005b; *Montelli et al.*, 2006b; *van der Hilst and de Hoop*, 2005], but we comment briefly on pragmatic aspects of such sensitivity kernels. We have been using approximations to full finite frequency kernels that are different from the approximation that has become known as the so-called "banana-doughnut kernel" [*Dahlen et al.*, 2000]. With the
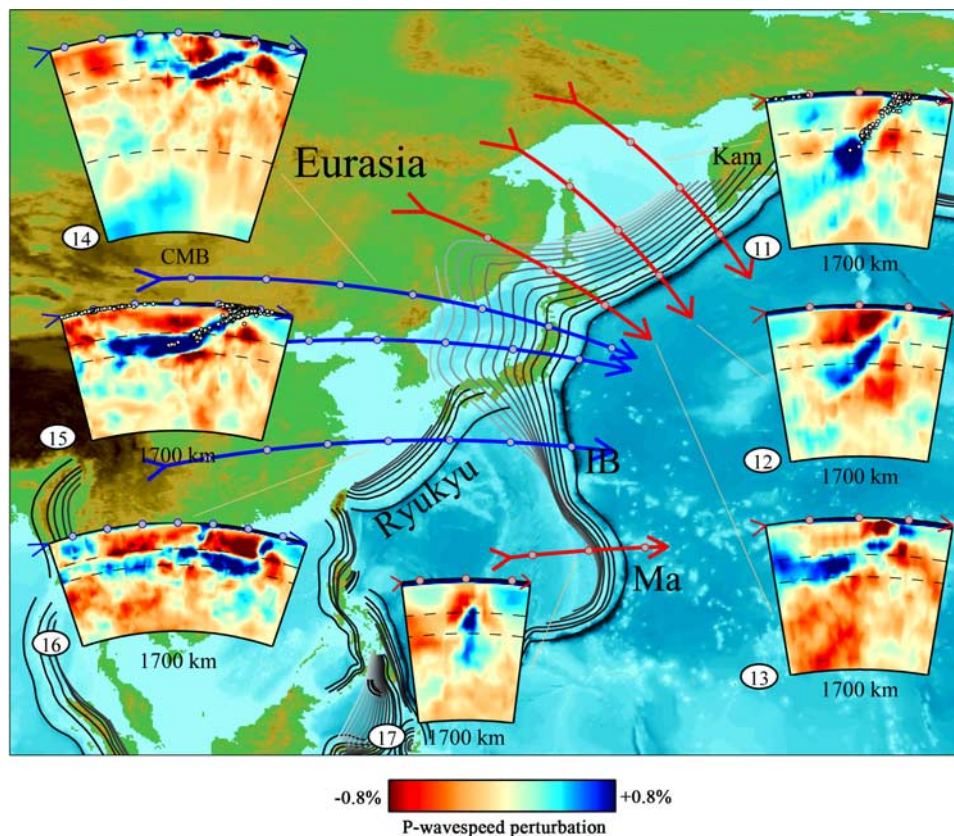
Figure 10. Northwestern Pacific and Philippine Sea subduction (Kam, Kamchatka; IB, Izu Bonin; Ma, Mariana).

data and the media considered, and in view of the fundamental non-uniqueness of this type linearized tomography (that is, a single-step linearization, with kernels calculated in a simple (quasi-homogeneous) background), this difference is not critical. Indeed, several studies [*Boschi et al.*, 2006; *Trampert and Spetzler*, 2006], including our own [e.g., *Kárason*, 2002; *van der Hilst and de Hoop*, 2006], have now shown that the effects of banana-doughnut kernels on tomographic images have, so far, been small (and perhaps insignificant). There are, however, practical differences between tomographic studies that affect the appearance of the models; these include the choice of data, parameterization, regularization, and misfit criteria. We stress that this does not mean that finite frequency effects are not important for tomography. On the contrary, for true multiresolution tomography with broad band waveforms more accurate theory and calculation is indeed needed [*de Hoop and van der Hilst*, 2005a; *Tromp et al.*, 2005; *de Hoop et al.*, 2006; *Chen et al.*, 2007].

[41] A detailed presentation and discussion of the mantle structures associated with mantle convec-

tion is beyond the scope of this paper, but we have given examples that illustrate the type of image of mantle structure that can be expected from our model.

[42] Questions as to whether the "narrow" slab-like features are an artifact of uneven (and selective) sampling of larger-scale structures (e.g., W. B. Hamilton, personal communication, 2004, 2006) can be addressed in several ways. *Van der Hilst et al.* [1997] showed, in their Figure 2, that even a decade ago data coverage would have been sufficient to resolve (with traveltimes) the type of long wavelength structure inferred from, for instance, the pioneering long-wavelength models by *Dziewonski and Woodhouse* [1987], and that very little small-scale structure is artificially induced by irregular data coverage and the use of a block parameterization. Furthermore, specific aspects of slab geometry have been studied by means of specially designed "hypothesis" tests [e.g., *Spakman et al.*, 1989; *van der Hilst*, 1995; *van der Hilst et al.*, 1997; *Ren et al.*, 2007]. As an example of the latter, auxiliary material Figure S3 shows results of inversions with synthetic data
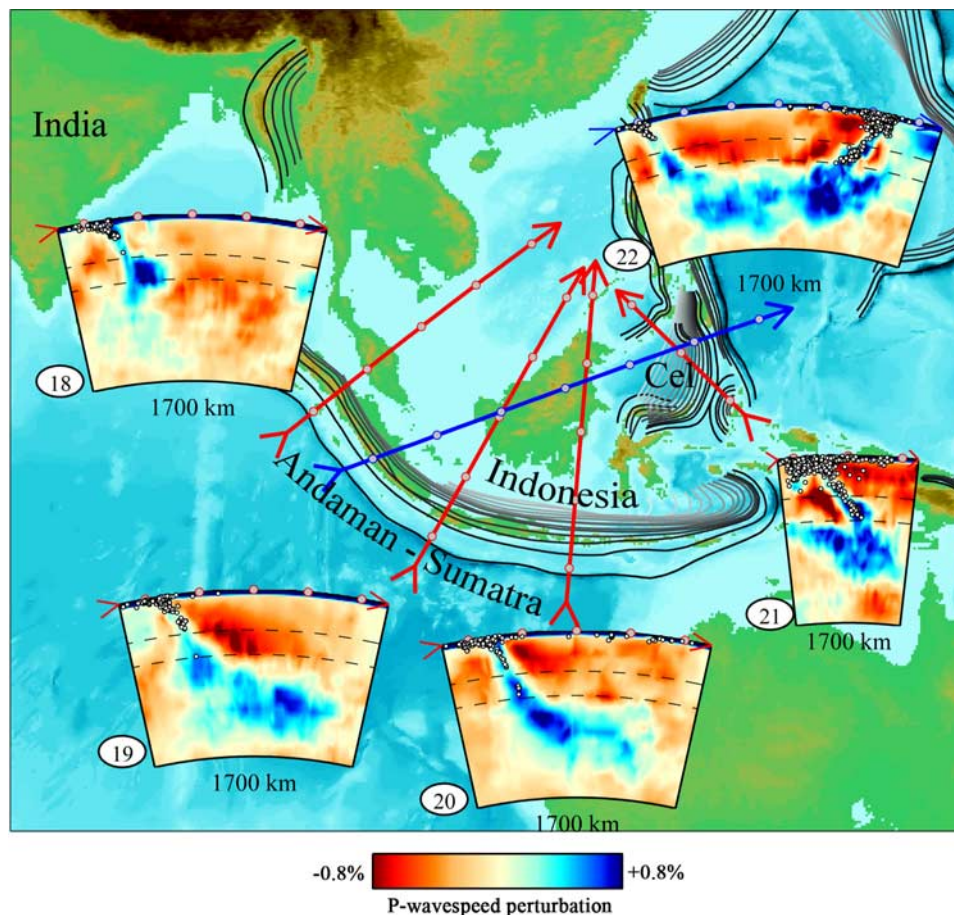
Figure 11. Andaman-Sumatra subduction (Cel, Celebes Sea).

calculated from input models that were designed to test the level of artificial mapping of upper mantle structures to lower mantle depths. From tests such as this we conclude that, in general, the deep mantle parts of the slab structures are well resolved and that they are not artifacts of uneven data coverage.

[43] As regards the "fate of the slabs," our new model confirms our previous conclusions [e.g., *van der Hilst et al.*, 1991, 1997; *Kárason and van der Hilst*, 2000; *Trampert and van der Hilst*, 2005] that there is significant variability in the depth to which slabs appear to sink. The images provide strong evidence for deep (present-day) subduction beneath Central America, Indochina, and segments of the northwestern and southwestern Pacific subduction systems. On the other hand, (present-day) stagnation of slab fragments in or near the upper mantle transition zone (say, 400–1000 km depth) is evident beneath parts of the Mediterranean, parts of Tonga, and, in particular, over large areas beneath the (northern) Philippine Sea plate and

SE Asia (largely in agreement with *Fukao et al.* [2001]).

[44] Given this variability, it is not useful to define a single "fate of the slab" as implied either by thermal boundary layer theory or by the canonical end-member models of layered or whole mantle convection. Indeed, in thermo-chemical convection the interplay between (1) a radial mixing gradient (with rapid overturn in the lower viscosity shallow mantle and sluggish convection in the higher-viscosity deeper mantle), (2) dynamical effects of phase transformations (which may produce local, transient layering [e.g., *van der Hilst and Seno*, 1993; *Thoraval et al.*, 1995]), (3) chemical effects of phase transformations (e.g., buoyancy of basalt fraction, local, transient compositional filtering [*Weinstein*, 1992]), and (4) realistic plates and plate motion and subduction histories (e.g., convergence rate, relative motion of the trench, age of plate at the trench, size of plate, length of trench, duration of subduction process), may well result in a system in which not all slabs behave the same or sink to the same depth and in which compositional het-
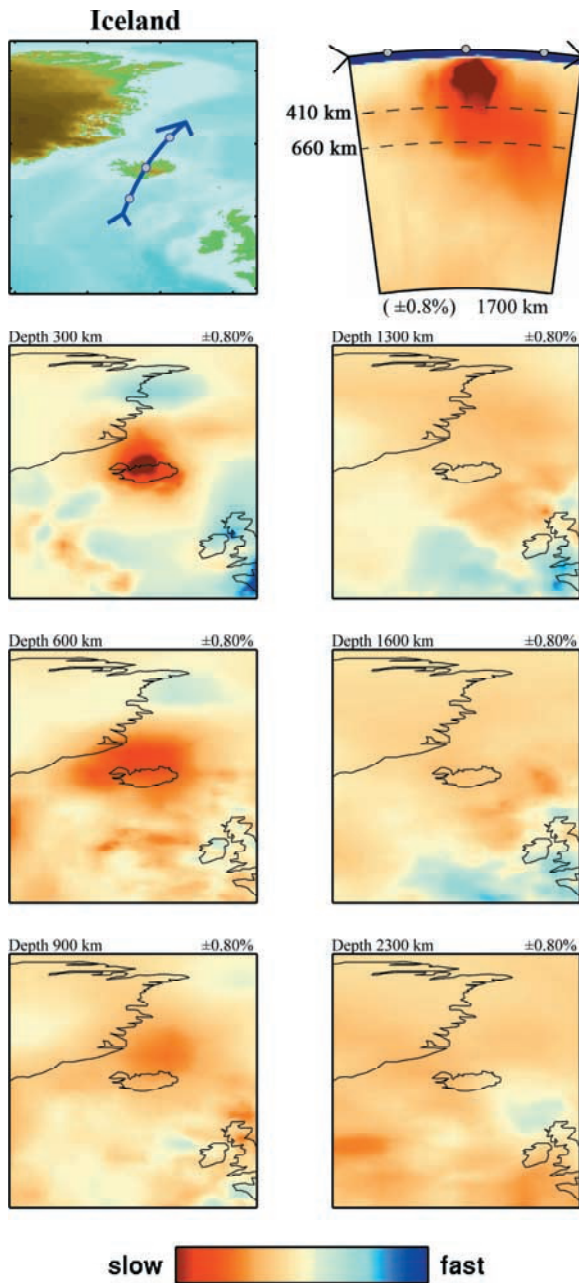
Figure 12. Mantle upwelling beneath Iceland. The cross section on the right upper corner shows *P* wave anomalies beneath Iceland from the surface down to 1700 km depth. The location of the cross section is shown in the subplot in the left upper corner. Other subplots show *P* wave speed perturbations map view at selected depths.

imaging of structure associated with downwellings has matured over the past decades, and further improvements may be incremental. For upwellings such maturation has not yet occurred. Tomography is revealing tantalizing wave speed anomalies that may be associated with thermal plumes or other types of upwelling, but limited data coverage continues to prevent adequate sampling of such structures. Indeed, resolution of the present-day controversies about "plume imaging" requires dramatic improvements in data coverage. This must be achieved (indirectly) through the use of better wave propagation theory and inversion methods (to allow the correct interpretation of a larger part of the recorded wavefield) and (directly)
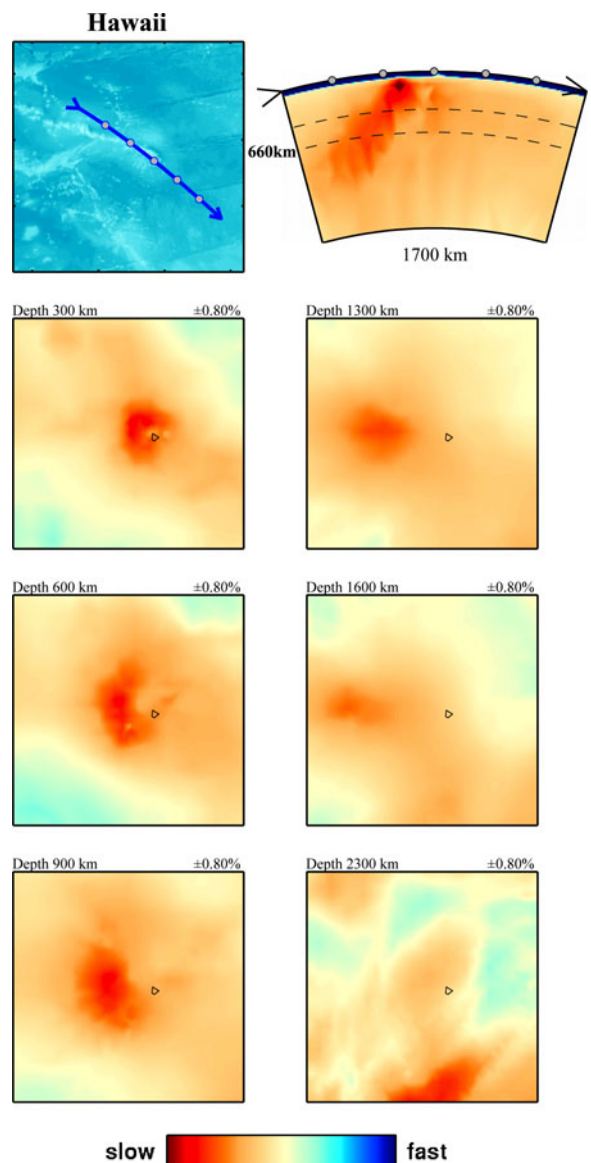

Figure 13. Mantle structure beneath Hawaii.

erogeneity is maintained self-consistently without "static" layering [see also *Albarède and van der Hilst*, 2002].

[45] Even if the implications for our understanding of mantle convection are still debated, tomographic
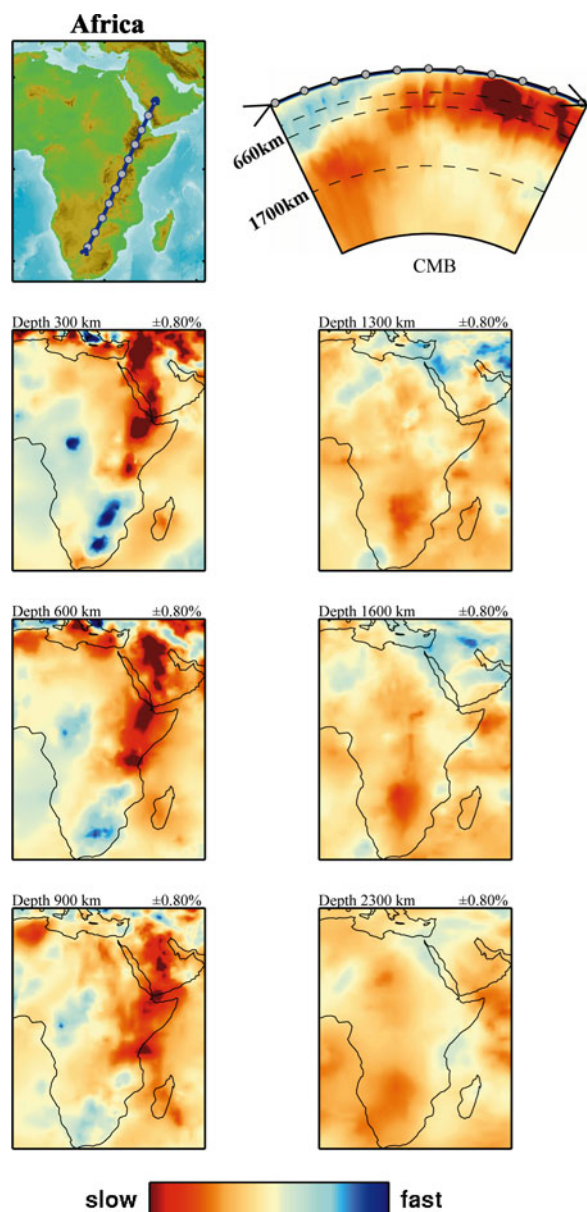
Figure 14. Mantle structure beneath Africa.

through the acquisition of data from denser seismograph networks on land and in, in particular, oceanic regions.

Acknowledgments

References

Abers, G. A., and S. W. Roecker (1991), Deep-structure of an arc-continent collision: Earthquake relocation and inversion for upper mantle P and S wave velocities beneath Papua New Guinea, *J. Geophys. Res.*, *96*, 6379–6401, doi:10.1029/91JB00145.

Albarède, F., and R. D. van der Hilst (2002), Zoned mantle convection, *Philos. Trans. R. Soc. London, Ser. A*, *360*, 2569–2592, doi:10.1098/rsta.2002.1081.

Bassin, C., G. Laske, and G. Masters (2000), The current limits of resolution for surface wave tomography in North America, *Eos Trans. AGU*, *81*(48), Fall Meet. Suppl., Abstract S12A-03.

Benoit, M. H., A. A. Nyblade, and J. C. VanDecar (2006), Upper mantle P wave speed variations beneath Ethiopia and the origin of the Afar Hotspot, *Geology*, *34*, 329–332, doi:10.1130/G22281.1.

Bijwaard, H., W. Spakman, and E. R. Engdahl (1998), Closing the gap between regional and global travel time tomography, *J. Geophys. Res.*, *103*(B12), 30,055–30,078, doi:10.1029/98JB02467.

Bolton, H., and G. Masters (2001), Travel times of P and S from global digital seismic networks: Implication for the relative variation of P and S velocity in the mantle, *J. Geophys. Res.*, *106*, 13,527–13,540, doi:10.1029/2000JB900378.

Boschi, L., and A. M. Dziewonski (1999), High- and low-resolution images of the Earth's mantle: Implications of different approaches to tomographic modeling, *J. Geophys. Res.*, *104*(B11), 25,567–25,594, doi:10.1029/1999JB900166.

Boschi, L., T. W. Becker, G. Soldati, and A. M. Dziewonski (2006), On the relevance of Born theory in global seismic tomography, *Geophys. Res. Lett.*, *33*, L06302, doi:10.1029/2005GL025063.

Burdick, S., C. Li, V. Martynov, T. Cox, J. Eakins, T. Mulder, L. Astiz, G. L. Pavlis, F. L. Vernon, and R. D. van der Hilst (2008), Upper mantle heterogeneity beneath North America from travel time tomography with global and *USArray* transportable array data, *Seismol. Res. Lett.*, in press.

Chen, P., T. H. Jordan, and L. Zhao (2007), Full 3-D waveform tomography: A comparison between the scattering-integral and adjoint-wavefield methods, *Geophys. J. Int.*, *170*, 175–181, doi:10.1111/j.1365-246X.2007.03429.x.

Courtillot, V., A. Davaille, J. Besse, and J. Stock (2003), Three distinct types of hotspots in the Earth's mantle, *Earth Planet. Sci. Lett.*, *205*, 295–308, doi:10.1016/S0012-821X(02)01048-8.

Dahlen, F. A., and G. Nolet (2005), Comment on "On sensitivity kernels for wave-equation transmission tomography" by M. V. de Hoop and R. D. van der Hilst, *Geophys. J. Int.*, *163*, 949–951.

Dahlen, F., S.-H. Hung, and G. Nolet (2000), Frèchet kernels for finite-frequency traveltimes - I. Theory, *Geophys. J. Int.*, *141*, 157–174, doi:10.1046/j.1365-246X.2000.00070.x.

de Hoop, M., and R. D. van der Hilst (2005a), On sensitivity kernels for 'wave equation' tomography, *Geophys. J. Int.*, *160*, 621–633, doi:10.1111/j.1365-246X.2004.02509.x.

de Hoop, M. V., and R. D. van der Hilst (2005b), Reply to comment by F.A. Dahlen and G. Nolet on "On sensitivity kernels for wave-equation transmission tomography,", *Geophys. J. Int.*, *163*, 952–955.

de Hoop, M. V., R. D. van der Hilst, and P. Shen (2006), Wave-equation reflection tomography: Annihilators and sensitivity

kernels, *Geophys. J. Int.*, *167*, 1332–1352, doi:10.1111/j.1365-246X.2006.03132.x.

Dziewonski, A. M. (1996), Earth's mantle in three dimensions, in *Seismic Modeling of Earth Structure*, edited by L. Boschi et al., pp. 507–572, Inst. Naz. di Geofis., Rome.

Dziewonski, A. M., and J. H. Woodhouse (1987), Global images of the Earth's interior, *Science*, *236*, 37–48, doi:10.1126/science.236.4797.37.

Engdahl, E. R., R. D. van der Hilst, and J. Berrocal (1995), Imaging of subducted lithosphere beneath South America, *Geophys. Res. Lett.*, *22*, 2317–2320, doi:10.1029/95GL02013.

Engdahl, E. R., R. D. van der Hilst, and R. Buland (1998), Global teleseismic earthquake relocation with improved travel times and procedures for depth determination, *Bull. Seismol. Soc. Am.*, *88*, 722–743.

Fukao, Y., M. Obayashi, H. Inoue, and M. Nenbai (1992), Subducting slabs stagnant in the mantle transition zone, *J. Geophys. Res.*, *97*, 4809–4822, doi:10.1029/91JB02749.

Fukao, Y., S. Widiyantoro, and M. Obayashi (2001), Stagnant slabs in the upper and lower mantle transition region, *Rev. Geophys.*, *39*, 291–323, doi:10.1029/1999RG000068.

Grand, S. P., R. D. van der Hilst, and S. Widiyantoro (1997), Global seismic tomography: A snapshot of convection in the earth, *GSA Today*, *7*, 1–7.

Gudmundsson, O., and M. Sambridge (1998), A regionalized upper mantle (RUM) seismic model, *J. Geophys. Res.*, *103*, 7121–7130, doi:10.1029/97JB02488.

Hafkenscheid, E., S. J. H. Buiter, M. J. R. Wortel, W. Spakman, and H. Bijwaard (2001), Modelling the seismic velocity structure beneath Indonesia: A comparison with tomography, *Tectonophysics*, *333*(1–2), 35–46, doi:10.1016/S0040-1951(00)00265-1.

Hafkenscheid, E., M. J. R. Wortel, and W. Spakman (2006), Subduction history of the Tethyan region derived from seismic tomography and tectonic reconstructions, *J. Geophys. Res.*, *111*(B8), B08401, doi:10.1029/2005JB003791.

Kárason, H. (2002), Constraints on mantle convection from seismic tomography and flow modeling, Ph.D. thesis, 228 pp., Mass. Inst. of Technol., Cambridge.

Kárason, H., and R. D. van der Hilst (2000), Constraints on mantle convection from seismic tomography, in *History and Dynamics of Plate Motion*, *Geophys. Monogr. Ser.*, vol. 121, edited by M. A. Richards, R. Gordon, and R. D. van der Hilst, pp. 277–288, AGU, Washington, D. C.

Kárason, H., and R. D. van der Hilst (2001), Tomographic imaging of the lowermost mantle with differential times of refracted and diffracted core phases (PKP, Pdiff), *J. Geophys. Res.*, *106*, 6569–6588, doi:10.1029/2000JB900380.

Kennett, B. L. N., E. R. Engdahl, and R. Buland (1995), Constraints on seismic velocities in the Earth from travel times, *Geophys. J. Int.*, *122*, 108–124, doi:10.1111/j.1365-246X.1995.tb03540.x.

Li, C., R. D. van der Hilst, and M. N. Toksöz (2006), Constraining P wave velocity variations in the upper mantle beneath Southeast Asia, *Phys. Earth Planet. Inter.*, *154*, 180–195, doi:10.1016/j.pepi.2005.09.008.

Masters, G. (1989), Low-frequency seismology and the three-dimensional structure of the Earth, *Philos. Trans. R. Soc. London, Ser. A*, *328*, 329–349, doi:10.1098/rsta.1989.0039.

McSweeney, T. J. (1995), Seismic constraints on core structure and dynamics, Ph.D. thesis, Univ. of Wash., Seattle.

Miller, M. S., B. L. N. Kennett, and G. S. Lister (2004), Imaging changes in morphology, geometry, and physical properties of the subducting Pacific plate along the Izu-

Bonin-Mariana arc, *Earth Planet. Sci. Lett.*, *224*(3–4), 363–370, doi:10.1016/j.epsl.2004.05.018.

Montagner, J. P. (1994), Can seismology tell us anything about convection in the mantle?, *Rev. Geophys.*, *32*(2), 115–137, doi:10.1029/94RG00099.

Montelli, R., G. Nolet, F. A. Dahlen, G. Masters, E. R. Engdahl, and S.-H. Hung (2004), Finite-frequency tomography reveals a variety of plumes in the mantle, *Science*, *303*(5656), 338–343, doi:10.1126/science.1092485.

Montelli, R., G. Nolet, F. A. Dahlen, and G. Masters (2006a), A catalogue of deep mantle plumes: New results from finite-frequency tomography, *Geochem. Geophys. Geosyst.*, *7*, Q11007, doi:10.1029/2006GC001248.

Montelli, R., G. Nolet, and F. A. Dahlen (2006b), Comment on 'Banana-doughnut kernels and mantle tomography' by van der Hilst and de Hoop, *Geophys. J. Int.*, *167*(3), 1204–1210, doi:10.1111/j.1365-246X.2006.03210.x.

Nolet, G. (1985), Solving or resolving inadequate and noisy tomographic systems *J. Comput. Phys.*, *61*, 463–482, doi:10.1016/0021-9991(85)90075-0.

Paige, C. C., and M. A. Saunders (1982), LSQR: An algorithm for sparse linear equations and sparse least squares, *ACM Trans. Math. Software*, *8*, 43–71, doi:10.1145/355984.355989.

Ren, Y., E. Stutzmann, R. D. van der Hilst, and J. Besse (2007), Understanding seismic heterogeneities in the lower mantle beneath the Americas from seismic tomography and plate tectonic history, *J. Geophys. Res.*, *112*, B01302, doi:10.1029/2005JB004154.

Replumaz, A., H. Kárason, R. D. van der Hilst, J. Besse, and P. Tapponnier (2004), 4-D evolution of SE Asia's mantle from geological reconstructions and seismic tomography, *Earth Planet. Sci. Lett.*, *221*(1–4), 103–115, doi:10.1016/S0012-821X(04)00070-6.

Spakman, W., and G. Nolet (1988), Imaging algorithms, accuracy and resolution in delay time tomography, in *Mathematical Geophysics: A Survey of Recent Developments in Seismology and Geodynamics*, edited by N. J. Vlaar, pp. 155–188, D. Reidel, Norwell, Mass.

Spakman, W., S. Stein, R. D. van der Hilst, and R. Wortel (1989), Resolution experiments for NW Pacific subduction zone tomography, *Geophys. Res. Lett.*, *16*, 1097–1101, doi:10.1029/GL016i010p01097.

Su, W. J., and A. M. Dziewonski (1992), On the scale of mantle heterogeneity, *Phys. Earth Planet. Inter.*, *74*, 29–54, doi:10.1016/0031-9201(92)90066-5.

Su, W. J., and A. M. Dziewonski (1995), Inner core anisotropy in three dimensions, *J. Geophys. Res.*, *100*, 9831–9852, doi:10.1029/95JB00746.

Thoraval, C., P. Machetel, and A. Cazenave (1995), Locally layered convection inferred from dynamic models of the Earth's mantle, *Nature*, *375*, 777–780.

Trampert, J., and J. Spetzler (2006), Surface wave tomography: Finite-frequency effects lost in the null space, *Geophys. J. Int.*, *164*, 394–400, doi:10.1111/j.1365-246X.2006.02864.x.

Trampert, J., and R. D. van der Hilst (2005), Towards a quantitative interpretation of global seismic tomography, in *Earth's Deep Mantle: Structure, Composition, and Evolution*, *Geophys. Monogr. Ser.*, vol. 160, edited by R. D. van der Hilst et al., pp. 47–62, AGU, Washington, D. C.

Tromp, J., C. Tape, and Q. Liu (2005), Seismic tomography, adjoint methods, time reversal and banana-doughnut kernels, *Geophys. J. Int.*, *160*, 195–216, doi:10.1111/j.1365-246X.2004.02453.x.

van der Hilst, R. D. (1990), Tomography with P, PP and pP delay time data and the three dimensional mantle structures below the Caribbean region, Ph.D. thesis, Utrecht Univ., Utrecht, Netherlands.

van der Hilst, R. D. (1995), Complex morphology of subducted lithosphere in the mantle beneath the Tonga trench, *Nature*, *374*, 154–157, doi:10.1038/374154a0.

van der Hilst, R. D., and M. V. de Hoop (2005), Banana-doughnut kernels and mantle tomography, *Geophys. J. Int.*, *163*, 956–961.

van der Hilst, R. D., and M. V. de Hoop (2006), Reply to comment by R. Montelli, G. Nolet, and F. A. Dahlen on "Banana-doughnut kernels and mantle tomography,", *Geophys. J. Int.*, *167*, 1211–1214, doi:10.1111/j.1365-246X.2006.03211.x.

van der Hilst, R. D., and E. R. Engdahl (1991), On ISC PP and pP data and their use in delay-time tomography of the Caribbean region, *Geophys. J. Int.*, *106*, 169–188, doi:10.1111/j.1365-246X.1991.tb04610.x.

van der Hilst, R. D., and P. Mann (1994), Tectonic implications of tomographic images of subducted lithosphere beneath northwestern South America, *Geology*, *22*, 451–454, doi:10.1130/0091-7613(1994)022<0451:TIOTIO>2.3.CO;2.

van der Hilst, R. D., and T. Seno (1993), Effects of relative plate motion on the deep structure and penetration depth of slabs below the Izu-Bonin and Mariana island arcs, *Earth Planet. Sci. Lett.*, *120*(3–4), 395–407, doi:10.1016/0012-821X(93)90253-6.

van der Hilst, R. D., and W. Spakman (1989), Importance of the reference model in linearized tomography and images of subduction below the Caribbean Plate, *Geophys. Res. Lett.*, *16*, 1093–1096, doi:10.1029/GL016i010p01093.

van der Hilst, R. D., E. R. Engdahl, W. Spakman, and G. Nolet (1991), Tomographic imaging of subducted lithosphere below northwest Pacific island, *Nature*, *353*, 37–43, doi:10.1038/353037a0.

van der Hilst, R. D., B. L. N. Kennett, D. Christie, and J. Grant (1994), Project SKIPPY explores the lithosphere and mantle beneath Australia, *Eos Trans. AGU*, *75*, 177–181, doi:10.1029/94EO00857.

van der Hilst, R. D., S. Widiyantoro, and E. R. Engdahl (1997), Evidence for deep mantle circulation from global tomography, *Nature*, *386*, 578–584, doi:10.1038/386578a0.

Weinstein, S. A. (1992), Induced compositional layering in a convecting fluid layer by an endothermic phase transition, *Earth Planet. Sci. Lett.*, *113*(1–2), 23–39, doi:10.1016/0012-821X(92)90209-E.

Widiyantoro, S., and R. D. van der Hilst (1996), Structure and evolution of lithosphere slab beneath the Sunda arc, Indonesia, *Science*, *271*, 1566–1570, doi:10.1126/science.271.5255.1566.

Woodward, R. L., and G. Masters (1991), Global upper mantle structure from long-period differential travel-times, *J. Geophys. Res.*, *96*(B4), 6351–6377, doi:10.1029/90JB01445.

Wysession, M. E. (1996), Large-scale structure at the core-mantle boundary from diffracted waves, *Nature*, *382*(6588), 244–248, doi:10.1038/382244a0.

Zhao, D. (2004), Global tomographic images of mantle plumes and subducting slabs: insight into deep Earth dynamics, *Phys. Earth Planet. Inter.*, *146*, 3–24, doi:10.1016/j.pepi.2003.07.032.

Zhao, L., and T. H. Jordan (1998), Sensitivity of frequency-dependent travel times to laterally heterogonous, anisotropic Earth structure, *Geophys. J. Int.*, *133*, 683–704, doi:10.1046/j.1365-246X.1998.00524.x.

Zhao, L., T. H. Jordan, and C. H. Chapman (2000), Three-dimensional Frèchet differential kernels for seismic delay times, *Geophys. J. Int.*, *141*(3), 558–576, doi:10.1046/j.1365-246x.2000.00085.x.